Large eddy simulation of spray and combustion characteristics with realistic chemistry and high-order numerical scheme under diesel engine-like conditions

Lei Zhou[1], Kai Hong Luo [1,2], Wenjin Qin[3],Ming,Jia[3], Shi Jin Shuai[1,4]

[1]Center for Combustion Energy, Tsinghua University, Beijing 100084, China

[2] Department of Mechanical Engineering, University College London, Torrington Place, London WC1E 7JE, UK

[3] School of Energy and Power Engineering，Dalian University of Technology，Dalian，116024

[4]State Key Laboratory of Automotive Safety and Energy, Tsinghua University, Beijing 100084, China

Abstract: The accuracy of large eddy simulation (LES) for turbulent combustion depends on suitably implemented numerical schemes and chemical mechanisms. In the original KIVA3V code, finite difference schemes such as QSOU (full name) and PDC (full name) cannot achieve good results or even computational stability when using coarse grids due to large numerical diffusion. In this paper, the MUSCL (Monotone Upstream-centered Schemes for Conservation Laws) differencing scheme is implemented into KIVA3V–LES code to calculate the convective term. In the meantime, Lu's n-heptane reduced 58-species mechanisms [Lu, 2011] is used to calculate chemistry with a parallel algorithm. Finally, improved models for spray injection are also employed. With these improvements, the KIVA3V-LES code is renamed as KIVALES-CP (Chemistry with Parallel algorithm) in this study. The resulting code was used to study the gas-liquid two phase jet and combustion under various diesel engine-like conditions in a constant volume vessel. The results show that using the MUSCL scheme can accurately capture the spray shape and fuel vapor penetration using even a coarse grid, in comparison with the Sandia experimental data. Similarly good results are obtained for three single-component fuels, i-Octane (C8H18), n-Dodecanese (C12H26), and n-Hexadecane (C16H34) with very different physical properties. Meanwhile the improved methodology is able to accurately predict ignition delay and flame lift-off length (LOL) under different oxygen concentrations from 10% to 21% with ambient density increasing from 14.8 kg/m^3 to 30.0 kg/m^3 and ambient temperatures from 850 K to 1300 K in a constant volume combustion chamber. With increasing oxygen concentration, the ignition delay time and consequently the flame LOL decrease, as the flame moves upstream as expected. On the other hand, reduction in the ambient temperature from 1000 K to 900 K retards the auto-ignition time and moves the burning location downstream under different oxygen concentrations.

Key words: large eddy simulation, high-order numerical schemes, liquid spray, detailed chemical mechanisms

Introduction

Liquid spray and combustion processes in an engine are extremely complex. They consist of a vast range of scales, ranging from chemical scales to the Kolomogrov scale and up to the cylinder diameter. Computational fluid dynamics (CFD) plays an important role in deeply understanding fuel spray and combustion characteristics and is being extensively used to design flow, spray and

combustion systems. Recently, thanks to the rapid increase in available computing power, Large Eddy Simulation (LES) has received increasing attention and become a very attractive tool for simulating complex spray and combustion processes in realistic systems.

In numerical simulations, high-order schemes are less frequently applied to complex systems, such as internal combustion (IC) engines，than to canonical configurations, such as channels. In a recent review, Rutland [1] pointed out that schemes of higher than second-order are difficult to be applied in IC engines due to the use of complex dynamic grids. However, high-order schemes can provide high-fidelity simulation and capture flow characteristics within a larger range of physical scales on a given grid. They also save computer memory and allow higher resolution simulations. Some recent studies have started to address this problem. Hori et al. [2] added a third-order cubic interpolated profile (CIP) scheme into KIVALES code and investigated spray features by using four different convection schemes. The results showed that low-order solutions can unphysically enlarge spray penetration, suppress vortex development and influence temperature distribution due to large numerical errors. A widely used LES code AVBP developed by CERFACS (Centre Européen de Recherche et de Formation Avancée en Calcul Scientifique) and IFP (Institut Français de Pétrole) also has a third-order spatial scheme, which has been applied to engine simulations [3-5] .

The MUSCL (Monotone Upstream-centered Schemes for Conservation Laws) scheme is one of the most popular finite difference schemes, which employs limiter techniques. The MUSCL series contain the second-order central scheme, the second-order upwind scheme and the third-order scheme or the Fromm scheme. In this study we have added the third-order upwind MUSCL scheme into KIVALES code to calculate the convective term in place of usual second-order or even first-order scheme.

Low temperature combustion (LTC) is a novel combustion concept for diesel engines that can

simultaneously reduce NOx and PM emissions using the exhaust gas recirculation (EGR) technique [6-9]. Many recent studies have focused on this combustion mode. Researchers at Sandia National Laboratories, for example, have conducted a lot of experiments investigating the liquid spray and combustion process under different oxygen concentrations (equivalent to EGR) in a constant volume combustion chamber. On their website [10] they provide high-fidelity measurement data such as spray shape, liquid and vapor penetration length, mixture-faction, ignition delay, flame lift-off length and soot emissions which form a comprehensive experimental database for spray and combustion models. In this study the n-heptane experiment data with different EGR conditions and other ambient conditions are used to validate the present spray and combustion models.

In order to understand the complex combustion process and obtain accurate temperature distribution, ignition delay time and flame lift-off length (LoL), a sufficiently detailed chemical mechanism is required. In the original KIVA3V code the eddy dissipation model is used, which does not give any detailed information about the combustion process. Kong et al. [11] interfaced the chemistry module of the CHEMKIN code with KIVA for simulation of homogeneous charge compression ignition engine processes. Simulations with detailed chemical kinetic mechanisms, however, will require huge computational resources. Thus some alternative methods were proposed such as chemistry tabulation. In this paper we develop an efficient way of implementing detailed chemical mechanisms in combination with parallel chemistry computation with MPI.

This paper presents a further development of the LES methodology by incorporating the high-order MUSCL scheme and parallel computation of detailed chemistry. The improved code, based on KIVA3D, is renamed as KIVALES-CP, and applied to simulate spray and combustion processes in a constant volume combustion chamber. A wide range of engine-like conditions have been simulated by varying the type of fuels, initial temperature, oxygen concentration and gas

density, as in the Sandia experiments. The three-dimensional numerical results show that the predicted flow velocity field, liquid spray structure and droplet distribution, ignition delay time and flame lift-off length are in good agreement with the Sandia experimental data.

2 Numerical Models

2.1 LES Equations

Applying the filtering operator to the conservation equations of mass, momentum, energy and species equations results in the following filtered equations for two-phase flows [12]:

Continuity Equation: $$\frac{\partial \overline{\rho}}{\partial t}+\frac{\partial \overline{\rho}\widetilde{u_j}}{\partial x_j}=\overline{\dot{\rho}^s} \tag{1}$$

Momentum Equations: $$\frac{\partial \overline{\rho}\widetilde{u_i}}{\partial t}+\frac{\partial}{\partial x_j}\left(\overline{\rho}\widetilde{u_i}\widetilde{u_j}-\overline{\tau_{ij}}-\tau_{ij}^{sgs}\right)=\overline{F_i^s} \tag{2}$$

Energy Equation: $$\begin{aligned}&\frac{\partial \overline{\rho}\widetilde{e}}{\partial t}+\frac{\partial \overline{\rho}\widetilde{u_j}\tilde{e}}{\partial x_j}+\overline{p}\frac{\partial \widetilde{u_j}}{\partial x_j}+\frac{\partial h_j^{sgs}}{\partial x_j}\\&+\frac{\partial \overline{q}_j}{\partial x_j}-\overline{\sigma_{ij}}\frac{\partial \widetilde{u_i}}{\partial x_j}-\Theta^{sgs}=\overline{\dot{Q}^s}+\overline{\dot{Q}^c}\end{aligned} \tag{3}$$

Species Equations: $$\begin{aligned}&\frac{\partial \overline{\rho}\widetilde{Y_m}}{\partial t}+\frac{\partial}{\partial x_j}\left(\overline{\rho}\widetilde{Y_m}\widetilde{u_j}-\overline{\rho D_m}\frac{\partial \widetilde{Y_m}}{\partial x_j}+\Phi_{j,m}^{sgs}\right)\\&=\overline{\dot{\rho}_m{}^s}+\overline{\dot{\rho}_m{}^c}\end{aligned} \tag{4}$$

where the filtered viscous stress tensor and the heat flux vector [where is the expression for the heat flux?] are approximated, respectively, as $\tau_{ij}^{sgs}=-2\overline{\rho}\upsilon_t\left(\widetilde{S}_{ij}-\frac{1}{3}\widetilde{S}_{kk}\delta_{ij}\right)+\frac{2}{3}\overline{\rho}k^{sgs}\delta_{ij}$, $\overline{q}_j$ is the filtered heat flux, $\overline{\dot{Q}^s}$ is the energy release per unit time due to spray, $\overline{\dot{Q}^c}$ is the chemical source term, $\dot{\rho}_m{}^s$ and $\dot{\rho}_m{}^c$ represent the density variation due to spray and chemistry, respectively. k^{sgs} is obtained by solving the subgrid turbulent kinetic energy equation:

$$\frac{\partial \overline{\rho}k^{sgs}}{\partial t}+\frac{\partial \overline{\rho}\widetilde{u}k^{sgs}}{\partial x_j}=P^{sgs}-D^{sgs}+\frac{\partial}{\partial x_j}\left(\frac{\overline{\rho}\nu_t}{\mathrm{Pr}_t}\frac{\partial k^{sgs}}{\partial x_j}\right)+\overline{\dot{W}^s} \tag{5}$$

Here, P^{sgs} and D^{sgs} represent subgrid kinetic energy production rate and dissipation rate, respectively.

The subgrid heat flux h_j^{sgs} and subgrid species mass flux $\Phi_{j,m}^{sgs}$ are closed by the gradient diffusion assumption. Details of this model can be found in reference [12].

2.2 The MUSCL method

The MUSCL method was proposed by Van Leer in 1979 [13]. In order to descript this method a one-dimensional scalar hyperbolic conservation law is given below:

$$\frac{\partial u}{\partial t}+\frac{\partial f(u)}{\partial x}=0, \quad (6)$$

where $f(u)$ represents a flux variable.

Based on a semi-discrete conservative scheme the above equation can be defined as follows:

$$\frac{\partial u_j}{\partial t}+\frac{1}{h}\left(\hat{f}_{j+1/2}-\hat{f}_{j-1/2}\right)=0 \quad (7)$$

where h is calculate by $h=x_{j+1}-x_j$, and $x_{j+1/2}=x_j+h/2$.

Through splitting the flux the MUSCL formulation can obtain different semi-discrete schemes, such as the second-order central scheme, and the second-order or third-order upwind scheme. Different schemes, which depend on the expression of $\hat{u}_{j+1/2,L}$ and $\hat{u}_{j+1/2,R}$, can be written in a unified form:

$$\hat{f}_{j+1/2}=f^{+}(\hat{u}_{j+1/2,L})+f^{-}(\hat{u}_{j+1/2,R}) \quad (8)$$

A more detailed form is

$$\hat{u}_{j+1/2,L}=u_j+\frac{1}{4}[(1-k)\bar{\delta}_x^{-}+(1+k)\bar{\delta}_x^{+}]u_j \quad (9)$$

$$\hat{u}_{j+1/2,R}=u_{j+1}-\frac{1}{4}[(1-k)\bar{\delta}_x^{+}+(1+k)\bar{\delta}_x^{-}]u_{j+1} \quad (10)$$

In the above equation, if the upwind direction is left of cell j, then $\hat{f}_{j+1/2}=f^{+}(\hat{u}_{j+1/2,L})$; otherwise $\hat{f}_{j+1/2}=f^{-}(\hat{u}_{j+1/2,R})$, $\bar{\delta}_x^{+}u_j=\min\mathrm{mod}(\delta_x^{+}u_j,2\delta_x^{-}u_j)$ and $\bar{\delta}_x^{-}u_j=\min\mathrm{mod}(\delta_x^{-}u_j,2\delta_x^{+}u_j)$. k is a factor [a constant?]. In this study, we use k=1/3. If there schemes are used simply, they will produce numerical oscillations. [How should the schemes be used without producing numerical oscillations?]

2.3 Eulerian-Lagrangian Momentum Coupling

The interaction between the Lagrangian (liquid) and the Eulerian (gas) phases is a very complex process especially in turbulent flow, which determines the fuel/air mixture formation. The two-phase coupling involves two aspects, “gas-to-liquid” and “liquid-to-gas” effects. In the “gas-to-liquid” coupling, the change of the droplet velocity in the computation domain is determined by the drag force $F_{i,d}$ acting on the droplet, which is calculated by the relative velocity between the liquid drop and the gas, as follow:

$$dv_{d,i}/dt = F_{i,d}/m_d = 0.375(\rho/\rho_l)|V_{rel}|/r_d\, V_{rel} C_D, \quad (11)$$

where $m_d = 4/3\pi\rho_l r_d^3$ is the droplet mass. V_{rel} is the relative velocity between the liquid droplet and the gas, ρ_l and r_d are the liquid droplet density and radius, respectively. C_D is the droplet drag coefficient, computed as follows:

$$C_D = \begin{cases} \dfrac{24}{\mathrm{Re}_d}(1+1/6\,\mathrm{Re}_d^{2/3}) & \mathrm{Re}_d < 1000 \\ 0.424 & \mathrm{Re}_d > 1000 \end{cases} \quad (12)$$

where Re_d is the droplet Reynolds number.

The relative velocity V_{rel} is a very important parameter and is calculated by gas velocity at the parcel [you need to explain a parcel.] positions $\tilde{u}_i$, turbulent dispersion velocity $u'_{p,i}$ (when considering turbulent effect on droplet)and droplet velocity $v_{d,i}$. The resulting formulation is $V_{rel} = \tilde{u}_i + u'_{p,i} - v_{d,i}$. In order to accurately simulate the gas phase effect on the liquid phase, the velocity interpolation model proposed by Nordin [14] was used, which employs an inverse distance weighting method based on the 8 vertices of the cell at the parcel location. More details can be found in reference [14].

The dispersion velocity $u'_{p,i}$ is randomly chosen from a Gaussian distribution with standard deviation $\sqrt{2/3k^{sgs}}$. k^{sgs} is the subgrid turbulent kinetic energy of the gas in the computational cell in which the droplet is located. The Gaussian distribution at sub-grid scale is given by $G(u'_{p,i}) = (4/3\pi k^{sgs})^{-3/2} \exp(-3u'^{2}_{p,i}/4k^{sgs})$.

In the "liquid-to-gas" coupling, the effect of liquid motion on gas phase is treated as the Lagrangian source terms of the Eulerian momentum equations of N-S Equations, $\overline{F_i^s}$ in Section 2.1. The momentum source $\overline{F_i^s}$ is calculated by summing the rate of change of momentum of all droplets in space and time. The expression is simply presented here for each computation cell:

$$\overline{F_i^s} = \sum_{per(i,j,k)} N_p \frac{4}{3}\pi\rho_l \left[\left(r^{n+1}\right)^3 v_d{}^{n+1} - \left(r^n\right)^3 v_d{}^n \right] \quad (13)$$

2.4 Spray source term model

In the sub-grid one equation turbulent kinetic energy equation (K-equation model), the spray source term $\overline{\dot{W}^s}$ is defined as [15]: $\overline{\dot{W}^s} \equiv -F_i u_i'$, where u_i' is the subgrid gas velocity and $F_i = \left(\sum_d F_{i,d}\right) \Big/ V_{cell}$ is the aerodynamic drag force.

In this study, the definition of the subgrid gas velocity is $u_i' \equiv u_i - \tilde{u}_i$.

where u_i and $\tilde{u}_i$ are the instantaneous and filtered velocities respectively.

So the spray source term can be expressed as $\overline{\dot{W}^s} \equiv -\left(\sum_d F_{i,d} u_i'\right) \Big/ V_{cell}$

In order to obtain the instantaneous velocity, an approximate deconvolution method (ADM) is employed [15]. With successive filtering, ADM leads to the following expression for the instantaneous velocity:

$$u_i \approx 3\tilde{u}_i - 3\tilde{\tilde{u}}_i + \tilde{\tilde{\tilde{u}}}_i \quad (14)$$

Accordingly, the subgrid gas velocity can be written simply as $u_i' = 2\tilde{u}_i - 3\tilde{\tilde{u}}_i + \tilde{\tilde{\tilde{u}}}_i$. Thus the final form of the spray source term can be written as $\overline{\dot{W}^s} = -\frac{3}{8}\frac{C_D}{V_{cell}} \sum_d \{ \frac{m_d \rho V_{rel}}{r_d \rho_l} \left(\tilde{u}_i + u_{p,i}' - v_{d,i}\right) \left(2\tilde{u}_i - 3\tilde{\tilde{u}}_i + \tilde{\tilde{\tilde{u}}}_i\right) \} \cdot$ (15)

A more detailed derivation of the spray source term can be found in the reference [15].

2.5 Spray breakup model

The breakup of a liquid fuel jet is a very complex physical phenomenon which is influenced by the aerodynamic liquid-gas interaction, the physical and thermal properties of the fuel and the ambient environment. In the present study, the Kelvin-Helmholtz and Rayleigh-Taylor (KH-RT) model [16] is used to predict the primary and subsequent secondary droplet breakup. In our previous study [???], we analyzed the effects of the different breakup models on the atomization and evaporation of liquid spray. The results show that the KH-RT is a good choice for liquid spray in large eddy simulation.

2.6 Combustion computation

In order to simulate the combustion process, parallel computation of detailed chemistry using the Message-Passing Interface (MPI) has been implemented into KIVALES to form a new code KIVALES-CP.. MPI allows for chemistry to be computed in parallel on multiple CPUs while the fluid dynamics is still simulated on a single processor. This process is accomplished at each computational time step. During the initial computation, CHEMKIN gas-phase library subroutines are called to read species information into KIVALES and to update the species parameters and calculate enthalpies . Once combustion occurs and chemical kinetic calculations start, KIVALES transfers information on the temperature, pressure and compositions of each cell to CHEMKIN, where chemical reactions are computed on a number of CPUs using decomposed uniform grids . This parallel process can be completed because that the information is local and each of the computational processors only needs to exchange information with its own group of cells [18]. At the last stage, the heat release and new species compositions are returned to KIVALES and the entire combustion computation cycle is completed.

The KIVALES-CP combustion model was used to calculate the heat release rate and change species density as follows [17]

$$\overline{\dot{Q}^c} = -\sum_{m=1}^{M} \overline{\dot{w}_m} \Delta h_{f,m} W_m, \quad \overline{\dot{\rho}_m^c} = \overline{\dot{w}_m} W_m, m = 1, \cdots M \qquad (16)$$

where $\overline{\dot{Q}^c}$ is heat released due to chemical reactions, $\Delta h_{f,m}$ is heat of formation of species m, $\overline{\dot{w}_m}$ and W_m are molar production rate and molecular weight of species m, $\overline{\dot{\rho}^c}_m$ is density of species m and M is total number of species, respectively.

Taking into consideration the turbulent kinetic energy effect, the molar production rate is expressed as [11]:

$$\overline{\dot{w}_m} = \frac{\overline{Y_m^*} - \overline{Y_m}}{\tau_{lam} + \chi \tau_{turb}}, \quad (17)$$

where $\overline{Y_m^*}$ is equilibrium concentration, $\overline{Y_m}$ is current concentration, τ_{lam} is a kinetic timescale $\tau_{lam} = (-Y_{fuel}^n / (Y_{fuel}^{n\prime} - Y_{fuel}^n))$, χ is the progress variable with a value ranging from 0 to 1 and calculated by $\chi = (1 - e^{-r}) / 0.632$, r is the ratio of the amount of products to that of total reactive species. τ_{turb} is a turbulent timescale. The final species concentration Y_i^{n+1} is calculated using the following equation [11]:

$$Y_i^{n+1} - Y_i^n = \frac{\tau_{lam}}{\tau_{lam} + \chi \tau_{turb}} (Y_i^{n\prime} - Y_i^n), \quad (18)$$

where, n+1 represents the new time, n represents the old time. Y_i^n and $Y_i^{n\prime}$ are the species concentrations before and after the CHEMKIN model is called.

The turbulent timescale in the original model for RANS was based on the eddy turnover time (k/ε). The new eddy characteristic time model for LES [19] is estimated by considering the Kolmogorov scale as below:

$\tau_{turb} = \left(\frac{\nu}{2\nu_t \overline{S_{ij}} \overline{S_{ij}}} \right)^{0.5}$, where S_{ij} is the rate of strain tensor for the resolved scale.

3. Numerical Conditions

In this study, the third-order MUSCL differencing scheme is employed to calculate the convection terms in LES. The Lagrangian dispersed-phase approach is used to describe the liquid phase. For spray modeling, the collision and coalescence model of O'Rourke is deployed. The atomization model is the KH-RT model [16]. No-slip wall boundary conditions are applied to all solid walls. The fully three-dimensional (3D) simulations were conducted in a cylindrical domain of 30 mm in diameter and 100 mm in height, as the base grid based on the studies of Bharadwaj et al. [15], Hori et al. [2] and Zhou et al. [20]. The overall computational grid has about 800,000 cells with the time step ranging from $1.*10^{-8}$ s to $1.*10^{-6}$ s. Table 1 shows the main experimental conditions by Lyle et al. [21,22]. All the results are obtained with the same models and model parameters. For the numerical calculation of combustion cases the massively parallel supercomputer in the Tsinghua High-Performance Computing Center is employed. For a typical case, 12 processors (Intel Xenon X5670 with 2.93GHz and 12MB cache) are used and run for about ten days.

4. Results and Discussion

4.1 Code validation in an engine assembly

In order to validate the MUSCL scheme in the new code KIVALES-CP, an axisymmetric piston-cylinder assembly of Morse et al. [23] with a fixed central valve, shown in Fig.1, was simulated in this work. The piston engine has a 150 mm bore, 60 mm stroke, and a 30 mm clearance height. The piston is driven in a simple harmonic motion at a speed of 200 rpm (the mean piston speed is 0.4m/s). For the engine configuration in Fig. 1, an overall computation mesh of 660,000 nodes is used. The mesh independence test was conducted in our previous work [24].

Fig.2a) presents the radial profiles of the axial mean velocity at crank angle of 36^0 and at locations of 8, 7 and 6 cm from the cylinder bottom using the QSOU and MUSCL schemes. For

Morse's engine, Laser-Doppler anemometry has been used to obtain radial profiles of axial mean velocity at different positions and crank angles. The mean velocity at a radius in each plane is obtained by averaging 20 points at the same radius in the azimuthal direction. In order to avoid the influence of the first cycle, Fig.2 a) shows the second cycle results. From the velocity distributions at three positions, it is clear that the axial mean velocity predictions using the MUSCL scheme are in a much better agreement with the experimental data than results from the QSOU scheme. In particular, the MUSCL scheme accurately predicted the peak value of the axial mean velocity at the axial plane of 7 cm while the QSOU scheme completely missed this peak. The different performances of the two schemes are because the third-order MUSCL scheme can reduce numerical diffusion in the discretization of the momentum equation and predict the velocity distribution more accurately than QSOU.

Fig.2 b) and c) present the radial profiles of the axial mean velocity at crank angle of 144^0 at axial locations of 8, 7 ,6, 5 and 4 cm from the cylinder bottom using the QSOU and MUSCL schemes. The MUSCL scheme gives better results at all positions except at 7 cm. Fig.2 b) and c) also show the cycle-to-cycle variation (CCV), which is difficult for RANS to obtain. For the results using the QSOU scheme it can be seen that the first-cycle results are very different from the results in the second and third cycles, indicating slow convergence of the numerical solution.

Overall, the above results indicate that the MUSCL scheme used in KIVALES-CP has the capability to capture accurately the spatial variations of in-cylinder velocities under engine-like conditions.

4.2 Spray simulation

The high-order difference scheme MUSCL is further validated in the spray simulation. A dense grid (about 6 million cells, cell size 0.25 mm) and a base grid (about 800,000 cells, cell size 0.5 mm) are

used. The QSOU scheme is tested on both grids while the MUSCL scheme is only used with the base grid. In the simulations, liquid penetration length is defined as the axial location which has accumulated 95% of injected fuel mass. Vapor penetration at any time is determined from the farthest downstream location of 0.1% fuel mass fraction. Figure 3 a) shows predicted and measured liquid spray and fuel vapor penetration with the MUSCL and QSOU schemes at an ambient temperature of 900 K for Case 1. [where is Case 1 defined?] Liquid penetration initially increases with time and then stabilizes at a quasi-steady value after about 0.1 ms after start of injection (ASOI) for all three cases. Compared to the experiment data, the liquid penetrations using the MUSCL scheme and QSOU scheme with the base grid have the same results, which are slightly lower than experiment data and results using the QSOU scheme with the dense grid. On the other hand, the vapor penetration predictions have significant differences among the two schemes even on the same base grid, especially at the later stage of spray. It can be seen that using the MUSCL scheme can predict a much more accurate result than the QSOU scheme on the base grid, which is in good agreement with experiment data and results using the QSOU scheme on a dense grid. Fig. 3 b) shows that using the MUSCL scheme with the base grid and the QSOU scheme with the dense grid can well describe the complex spray structure including the spray penetration length and vapour mixture fraction. As for the results of QSOU with the base grid the unsteady turbulence behavior and diffusion are suppressed. In contrast, using the MUSCL scheme gives close agreement with the Sandia data due to decreased numerical diffusion and thus more accurate flow momentum. In terms of computational cost for Case 1, the QSOU with the base grid needs 7 hours of simulation time, the MUSCL with the base grid 8 hours, and the QSOU with dense grid 72 hours on one processor, as listed in Table 2.

The gas-liquid flow is a very complex phenomenon and in order to identify the liquid spray structures more clearly, the Q criterion [25] was used in the present work. In the Q criterion, the

positive second invariant of the velocity gradient tensor (∇v) is used to describe the turbulent vortex structure. A large and positive Q value implies a strong vortex region. The second invariant Q can be written as $Q = \frac{1}{2}\left(\|\Omega\|^2 - \|S\|^2\right)$, where S and Ω are the symmetric and anti-symmetric components of ∇v defined as $S = \frac{1}{2}\left(\nabla v + (\nabla v)^t\right)$ and $\Omega = \frac{1}{2}\left(\nabla v - (\nabla v)^t\right)$ respectively.

Figure 4 presents the influence of the convective schemes on the evolution of vortex with injection time at 1.5ms ASOI for Case 1. It can be seen from Fig.4 that small eddy structures are shown with the increase of Q value and strong eddies can be captured by the present models. It is noted that unlike QSOU with the base grid, using MUSCL with the base grid can distinguish more small eddies and capture strong vortex regions, even at the Q value of $4.5*10^8$. Thus in this study, the MUSCL with the base grid is adopted to capture sufficiently detailed flow structures at a relatively low computational cost.

In order to validate the MUSCL scheme further, the three single-component fuels, i-Octane (C8H18), n-Dodecanese (C12H26), and n-Hexadecane (C16H34) are simulated, which have different boiling points and liquid densities. The three types of fuels are selected to represent low boiling point, medium boiling point and high boiling point fuel, respectively. Figure 5 shows predicted results using LES with MUSCL and QSOU,[I cannot see any results using QSOU!] compared with experimental images obtained by Mie-scattered light and shadowgraph method at the end of injection of 1.82ms ASOI for case 2 [26]. For the simulation results, the black dots represent liquid phase, while the bright area in experimental image means the liquid phase area. It can be seen from the comparison in Fig.5 that predicted liquid penetration lengths with MUSCL are similar to the experiment results and obviously better than the results of QSOU. The QSOU fails to predict the change of liquid penetration length against liquid density. Note that decrease in the carbon number in a fuel can result in reduction in the penetration length of liquid phase, owing to decrease in boiling

296 point and liquid density and promotion of evaporation at the same ambient temperature. The
297 decrease in the carbon number also can lower the molecular weight, liquid density and boiling
298 temperature, and decrease fuel vapor concentration in each cell. Thus for C8H18, it is easy to
299 evaporate and has enough time to diffuse in space, unlike fuel C16H34. The experiment in Fig.5 also
300 demonstrates this phenomenon. Quantitative results of liquid phase length for different liquid density
301 are presented in Fig.6. It can be seen that predicted results with MUSCL are in excellent agreement
302 with experimental data and have similar trends with increasing liquid density, although the
303 agreement for fuel C16H34 is not perfect. The QSOU scheme, on the other hand, has consistently
304 overpredicted the liquid phase length. Overall, the present MUSCL scheme can predict liquid spray
305 characteristics accurately under different fuel boiling points and liquid densities.

306 **4.3 Reaction case**

307 Chemistry is an essential factor influencing the ignition process. In order to simulate the
308 heptane spray and combustion process, seven chemistry mechanisms used frequently in internal
309 combustion engine are firstly investigated in terms of the auto-ignition delay time at two oxygen
310 concentrations in a constant volume vessel. The low oxygen concentration cases represent exhaust
311 gas recirculation (EGR) conditions. The detailed results are listed in Table 3. From the results it can
312 be seen that for 21% oxygen concentration, all the chemical mechanisms except Ra's give a
313 reasonable prediction of the auto-ignition delay time in comparison with the experiment data.
314 However, for the 12% oxygen concentration condition the auto-ignition delay time predicted by only
315 LU-88 and LU-55 chemical mechanisms is consistent with the experiment data. Note that the two
316 accurate mechanisms are derived from a two-stage directed relation graph (DRG) [27] starting from
317 the detailed LLNL mechanism with 561 species and 2539 elementary reactions [28]. Thus, the

LU-55 mechanism is chosen to simulate the combustion process under different oxygen concentrations, ambient densities and ambient temperatures.

In this section, the flame lift-off length (LoL) and ignition delay time are predicted and discussed using KIVALES-CP with the MUSCL scheme and Lu's n-heptane reduced 58-species mechanism under different oxygen concentrations (EGR ratios), ambient temperatures and ambient gas densities. These conditions are of relevance to the low temperature combustion (LTC) strategy for HCCI engines. Note that this mechanism needs to invoke a mechanism-specific subroutine CKWYP to compute the species production rates including quasi steady state (QSS) species. Figure 7 shows the temperature and OH radical distributions at 2.0ms ASOI compared with Sandia experimental images. In the experimental images, the red color field represents the high temperature region. In the predicted results, the black color indicates the liquid phase while the white dash-dot line represents the flame lift-off position. It can be seen that the temperature in the reaction zones generally increases with increasing oxygen concentration (that is, less EGR). Note that, for oxygen concentration of 10% the chamber temperature is very low and the burning is barely visible. Simultaneously the OH radical concentration also increases with increasing oxygen concentration, as chemical reactions become more intense. And the distributions of high OH radical concentrations are consistent with the high temperature zones.

Figure 8 quantitatively predicts the effect of the oxygen concentrations on ignition delay time and flame lift-off length (LO) using the present models in KIVALES-CP in comparison with measured data under ambient initial temperatures of 900 K and 1000 K. As the size of the LES domain is different from the experiment setup, so following the practice in [5] the ignition delay time in the simulations is defined as the point in time when the temperature in the domain reaches half of the peak temperature in the entire combustion process in the domain. The lift-off length is also defined

as the location where the temperature reaches half of the peak temperature in the entire combustion process in the domain. With increasing oxygen concentration, the ignition delay time and consequently the flame LOL decrease, as the flame moves upstream as expected. On the other hand, when the ambient temperature is decreased from 1000 K to 900 K, the auto-ignition time is retarded and the burning location is moved downstream under different oxygen concentrations. In fact, for the ambient temperature of 900 K and oxygen concentration of 10% case, the combustion temperature is so low that it is not easy to capture accurately the combustion characteristics and consequently there is a considerable deviation from the Sandia data. Overall, the trends of ignition delay time and LOL variation against the ambient temperature and oxygen concentration obtained by the improved LES are consistent with the Sandia experimental data. Note that, comparing Fig. 7 and Fig. 8, the definition of flame LOL using the half-temperature method in the work is the same as that of using OH radical distribution method.

Ignition and flame location are heavily dependent on the mixture formation. The present LES method with the MUSCL scheme can capture the vapor distribution more accurately as shown in section 4.3. Thus, on the whole the temperature field variations with oxygen concentration are accurately predicted by the present method compared with Sandia images. An interesting phenomenon in LTC that decreasing oxygen concentration or increasing EGR can effectively retard burning and decrease combustion temperature can also be obtained by the KIVALES-PC code with the MUSCL scheme and Lu's n-heptane reduced 58-species mechanism.

Figure 9 presents the effect of the oxygen concentration on ignition delay time under ambient density of 30.0 kg/m^3. The same trend of ignition delay time variation with an increase in the oxygen concentration is obtained, as compared with that under ambient density of 14.8 kg/m^3. At oxygen concentrations of 8% and 10% the computed ignition delay time is lower than the experiment data.

This may be due to the fact that the combustion temperature is so low under these conditions that there are larger errors in the ignition delay time determined by both the simulation and experimental data. In Fig.10 it can be seen that increasing ambient density causes the flame to move upstream under the same ambient temperature of 1000 K and oxygen concentration of 15%. Combined with Fig.8 and Fig.9, it is clear that an ambient density increase from 14.8 kg/m^3 to 30.0 kg/m^3 leads to a decrease in flame LOL from 27 mm to 11 mm and in ignition delay time from 0.75 ms to 0.38 ms. This phenomenon can be explained by the enhanced reactivity of heptane under higher pressure, which can only be simulated reliably with sufficiently detailed chemical mechanisms such as LU-55. The above numerical simulations demonstrate that the improved LES methedology can capture quantitative differences in the ignition delay and flame LOL due to different ambient densities, in good agreement with Sandia data.

Fig.11 presents the ignition delay time over a very wider range of ambient temperatures from 850 K to 1300 K under oxygen concentration of 21% and ambient density of 14.8 kg/m^3. It illustrates that increased ambient temperature results in decreased ignition delay time due to fast evaporation and mixture formation, followed by increased chemical reactivity simultaneously. A good agreement between the LES predictions and the Sandia experimental data has been obtained over a wide range of ambient temperatures except at 850 K and 1300 K. At the low ambient temperature of 850 K, the chemical reactivity is low and the combustion temperature is also low, which leads to increased difficulty in accurately determining the ignition delay time in both experiment and simulation. This is the same situation as with the low oxygen concentration shown in Figs. 8 and 9. As for the high ambient temperature of 1300 K, the experimental data shows almost the same ignition delay time under 1200 K and 1300 K, respectively, which is abnormal. The increased discrepancy with the LES prediction under the ambient temperature of 1300 K may be due to an experimental error.

5 Conclusions

In this paper, improved large eddy simulation (LES) with high-order numerical schemes and detailed chemical mechanisms has developed and applied to study liquid fuel spray and turbulent combustion in a constant volume chamber. The third-order MUSCL scheme is employed, which leads to enhanced numerical accuracy. Meanwhile, for combustion simulation, an n-heptane reduced mechanism (58 species, 387 reactions) is implemented with parallel computation using Message-Passing Interface (MPI). The resulting KIVALES-CP code has been validated in various flow/spray/flame configurations and superior performance is demonstrated over the KIVALES base code.

In order to validate the MUSCL numerical scheme, an axisymmetric piston-cylinder engine assembly is used. It is shown that the use of the MUSCL scheme can reduce numerical diffusion and thus obtain better predictions of axial mean velocity at different locations than using the QSOU scheme, as compared with the experiment data. In the diesel spray case, simulation results with QSOU show that eddy structures in the gas phase are suppressed by numerical diffusion. And it overpredicts the vapor length compared with the experiment data, unless very fine grid is used, at a much higher computational cost. In contrast, using the MUSCL scheme with the coarse base grid can give an excellent agreement with the Sandia data. In addition, the results using the MUSCL scheme capture more small eddies and strong vortex regions, even at the Q value of $4.5*10^8$. The MUSCL scheme can capture the same trend as the experiment data for different hydrocarbon fuels with different boiling points and liquid densities. For reacting cases, using parallel computation via MPI can significantly reduce computational time. The improved LES incorporating the MUSCL scheme, subgrid spray models and realistic chemical mechanisms for heptane in KIVALES-CP predicts qualitatively and quantitatively correct results in agreement with experimental under diesel

engine-like conditions, except at some special points where experimental errors are also large. The flame lift-off length and ignition delay time reduce in response to increase in ambient temperature, ambient density and oxygen concentration, respectively. In summary, the improved LES methodology presented in this study has been successful in predicting the velocity distribution, droplet and vapor phase distribution and combustion characteristics under a very wide range of conditions.

6 Acknowledgements

The work at the Center for Combustion Energy of Tsinghua University was supported by the UK Royal Academy of Engineering, China Postdoctoral Science Foundation (2012M510437) and Key Program of National Natural Science Fund (51036004). The numerical simulations are conducted on the “Explorer 100” High-Performance Computer of Tsinghua National Laboratory for Information Science and Technology. The first author is thankful to Dr. Xianming Wang for his help and advice on the high-order schemes.

Reference

[1] Rutland, C. Large-eddy simulations for internal combustion engines–a review, International Journal of Engine Research,2011, 12 (5), pp. 421-451.

[2] Hori, T., Kuge, T., Senda, J.,Fujimoto, H., Large Eddy Simulation of Diesel Spray Combustion with Eddy-Dissipation Model and CIP Method by Use of KIVALES, SAE Paper 2007-01-0247, 2007

[3] Moureau, V., Barton, I., Angelberger, C.,Poinsot, T. Towards large eddy simulation in internal-combustion engines: simulation of a compressed tumble flow, SAE Paper 2004, 2004-01-1995.

[4] Thobois, L., Lauvergne, R., Poinsot, T.,Cerfacs, P., Using LES to investigate reacting flow physics in engine design process, 2007-01-0166, 2007

[5] Bekdemir, C., Somers, L., de Goey, L., Tillou, J.,Angelberger, C. Predicting diesel combustion characteristics with large-eddy simulations including tabulated chemical kinetics, Proceedings of the Combustion Institute,2013, 34 (2), pp. 3067-3074.

[6] Musculus, M.P., Miles, P.C.,Pickett, L.M. Conceptual models for partially premixed low-temperature diesel combustion, Progress in Energy and Combustion Science,2013, 39 (2), pp. 246-283.

[7] Taghavifar, H., Taghavifar, H., Mardani, A.,Mohebbi, A. Modeling the impact of in-cylinder combustion

parameters of DI engines on soot and NOx emissions at rated EGR levels using ANN approach, Energy Conversion and Management,2014, 87 (0), pp. 1-9.

[8] Imtenan, S., Varman, M., Masjuki, H.H., Kalam, M.A., Sajjad, H., Arbab, M.I.,Rizwanul Fattah, I.M. Impact of low temperature combustion attaining strategies on diesel engine emissions for diesel and biodiesels: A review, Energy Conversion and Management,2014, 80 (0), pp. 329-356.

[9] Jing, W., Roberts, W.L.,Fang, T. Spray combustion of Jet-A and diesel fuels in a constant volume combustion chamber, Energy Conversion and Management,2015, 89 (0), pp. 525-540.

[10] Pickett LM. Engine combustion network, "http://www.sandia.gov/ecn."

[11] Kong, S.-C., Marriott, C.,Reitz, R.D., Modeling and experiments of HCCI engine combustion using detailed chemical kinetics with multidimensional CFD, SAE: 2011-01-1026, 2001

[12] Sone, K.,Menon, S. Effect of subgrid modeling on the in-cylinder unsteady mixing process in a direct injection engine, Journal of Engineering for Gas Turbines and Power-Transactions of the Asme,2003, 125 (2), pp. 435-443.

[13] Van Leer, B. Towards the ultimate conservative difference scheme. II. Monotonicity and conservation combined in a second-order scheme, Journal of computational physics,1974, 14 (4), pp. 361-370.

[14] Nordin, N. The KIVA Jumpstation [Online]. Available: http://www.tfd.chalmers.se/~nordin/KJS/.

[15] Bharadwaj, N., Rutland, C.,Chang, S. Large eddy simulation modelling of spray-induced turbulence effects, International Journal of Engine Research,2009, 10 (2), pp. 97-119.

[16] Patterson, M.A.,Reitz, R.D., Modeling the Effects of Fuel Spray Characteristics on Diesel Engine Combustion and Emissions, SAE Paper 980131, 1998

[17] Jonnalagedda, S., Nguyen, T., Zhou, B.,Sobiesiak, A., Numerical Investigation of HCCI Combustion in an IDI Type Diesel Engine Fueled with Isooctane, SAE 2011-01-1181, 2011

[18] Senecal, P., Pomraning, E., Richards, K., Briggs, T., Choi, C., McDavid, R.,Patterson, M. Multi-dimensional modeling of direct-injection diesel spray liquid length and flame lift-off length using CFD and parallel detailed chemistry, SAE transactions,2003, 112 (3), pp. 1331-1351.

[19] Jagus, K.,Jiang, X. Large Eddy Simulation of Diesel Fuel Injection and Mixing in a HSDI Engine, Flow, turbulence and combustion,2011, 87 (2-3), pp. 473-491.

[20] Zhou, L., Xie, M., Jia, M.,Zhou, Q., Influences of subgrid turbulent kinetic energy and turbulent dispersion on the characteristics of fuel spray, SAE 2011-01-1839 2011

[21] Pickett, L.M., Genzale, C.L., Bruneaux, G., Malbec, L.-M., Hermant, L., Christiansen, C.,Schramm, J. Comparison of diesel spray combustion in different high-temperature, high-pressure facilities, SAE Int. J. Engines,2010, 3 (2), pp. 156-181.

[22] Idicheria, C.A.,Pickett, L.M. Effect of EGR on diesel premixed-burn equivalence ratio, Proceedings of the Combustion Institute,2007, 31 (2), pp. 2931-2938.

[23] Morse, A.P., Whitelaw, J.H.,Yianneskis, M.; Imperial College Dept. Mech.: 1978.

[24] Qin, W.J., Xie, M.Z., Jia, M.,Zhou, L. Large eddy simulation of turbulent flows and cyclic variations in internal combustion engine, Journal of Engineering Thermophysics,2011, 32 (1), pp. 268-271.

[25] Chakraborty, P., Balachandar, S.,Adrian, R.J. On the relationships between local vortex identification schemes, Journal of Fluid Mechanics,2005, 535 (1), pp. 189-214.

[26] Myong, K.-J., Suzuki, H., Senda, J.,Fujimoto, H. Evaporation characteristics of multi-component fuel, Fuel,2006, 85 (17), pp. 2632-2639.

[27] Lu, T.,Law, C.K. Linear time reduction of large kinetic mechanisms with directed relation graph:n-Heptane and iso-octane, Combustion and Flame,2006, 144 (1), pp. 24-36.

[28] Curran, H., Gaffuri, P., Pitz, W.J.,Westbrook, C.K. A comprehensive modeling study of n-heptane oxidation, Combustion and flame,1998, 114 (1-2), pp. 149-177.

[29] Liu, S., Hewson, J.C., Chen, J.H.,Pitsch, H. Effects of strain rate on high-pressure nonpremixed n-heptane

autoignition in counterflow, Combustion and flame,2004, 137 (3), pp. 320-339.
[30] Liu, Y.-D., Jia, M., Xie, M.-Z.,Pang, B. Enhancement on a Skeletal Kinetic Model for Primary Reference Fuel Oxidation by Using a Semidecoupling Methodology, Energy & Fuels,2012, 26 (12), pp. 7069-7083.
[31] Yoo, C.S., Lu, T., Chen, J.H.,Law, C.K. Direct numerical simulations of ignition of a lean n-heptane/air mixture with temperature inhomogeneities at constant volume: Parametric study, Combustion and Flame,2011, 158 (9), pp. 1727-1741.
[32] Patel, A.,Kong, S.-C., "Development and validation of a reduced reaction mechanism for HCCI engine simulations," SAE paper 2004-01-0558, 2004.
[33] Ra, Y.,Reitz, R.D. A reduced chemical kinetic model for IC engine combustion simulations with primary reference fuels, Combustion and Flame,2008, 155 (4), pp. 713-738.
[34] Tsurushima, T. A new skeletal PRF kinetic model for HCCI combustion, Proceedings of the Combustion Institute,2009, 32 (2), pp. 2835-2841.

Figures

Fig. 1 Axisymmetric piston-cylinder assembly of Morse et al.

Fig. 2 Distribution of axial mean velocity with radial distance from axial at crank angle of ATDC 36º and ATDC 144º

Fig.3 Measured and predicted penetration length and fuel mass fraction at 1.5 ms for liquid and vapor phase using MUSCL and QSOU under base grid(about 800,000 cells) and dense grid (about 6 million cells) for Case 1

Fig. 4 The evolution of vortex field with injection time at 1.5ms after start of injection for MUSCL and QSOU under base grid (case 1)

Fig.5 Comparison of predicted results using LES and experiment image by mie-scattered light and shadowgraph at the end of injection of 1.82ms for case 2

Fig.6 Change in liquid phase length obtained through simulation using MUSCL and QSOU and experiment at different fuel density for case 2.

Fig.7 Measured and predicted temperature and OH contours under different EGR at 2.0ms ASOI for Case 3

(ambient density=14.8 kg/m^3, ambient initial temperature=1000 K). Dashed white line is flame lift-off length.

Fig.8 Measured and predicted ignition delay and flame lift-off length at different EGR for Case 3 (ambient density=14.8kg/m^3, ambient initial temperature=900 K and 1000K)

Fig.9 Measured and predicted ignition delay time under different oxygen concentration (ambient density=30.0 kg/m^3, ambient initial temperature=1000K).

Fig.10 Influence of ambient density on temperature distribution under oxygen concentration of 15% and ambient temperature of 1000 K

Fig.11 Measured and predicted ignition delay time at different ambient temperature under oxygen concentration of 21% (ambient density=14.8 kg/m^3)

Tables

Table 1 Experimental conditions

Case	Fuel	Hole diameter（mm）	Injection duration（ms）	Injection pressure（MPa）	Fuel mass（mg）	fuel temperature（K）	ambient gas oxygen	Ambient density（kg/m^3）	Ambient temperature （K）	Ref.
Case 1	C12H26	0.09	1.54	150	3.5	363	0% (non-reacting)	22.8	900	[21]
Case 2	C8H18 C12H26 C16H34	0.2	1.82	72	12	368	0% (non-reacting)	15.0	700	[26]

Case 3	C7H16	0.1	6.8	150	17.8	373	10%~21% (reacting)	14.8, 30.	850-1300	[22]

548

549 Table 2 Comparison of computation time using different numerical schemes

	Base grid	Dense grid
QSOU	7 CPU hours	72 CPU hours
MUSCL	8 CPU hours	80 CPU hours

550

551

552 Table 3 The ignition delay time at two oxygen concentrations (21% and 12%) using seven reduced n-heptane

553 mechanisms.

	Ignition delay time predicted by different reduced chemical mechanisms (Unit: ms)							
	LIU-SL	LIU-YD	LU-88	Patel	Ra	TS	Lu-55	Exp.data
Species numbers	44[29]	37[30]	88[31]	29[32]	41[33]	35[34]	55[31]	N/A
21% O_2	0.65	0.60	0.57	0.61	1.0	0.64	0.57	0.53
12% O_2	1.2	1.48	0.90	1.3	2.7	1.3	0.92	0.95

554

555

556

557

558

559

560

561

562

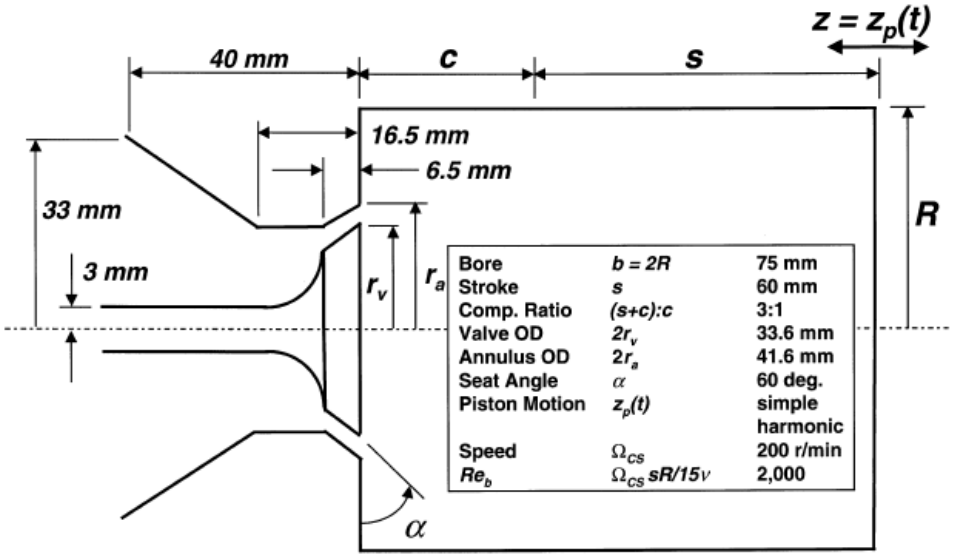

Fig. 1 Schematic of the axisymmetric piston-cylinder assembly of Morse et al. [23]

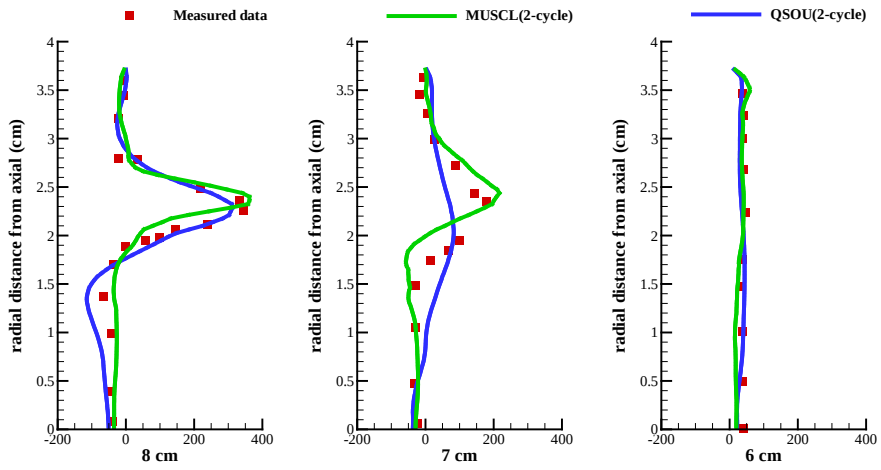

577 Axial mean velocity (cm/s)

578 2 a) ATDC 36°

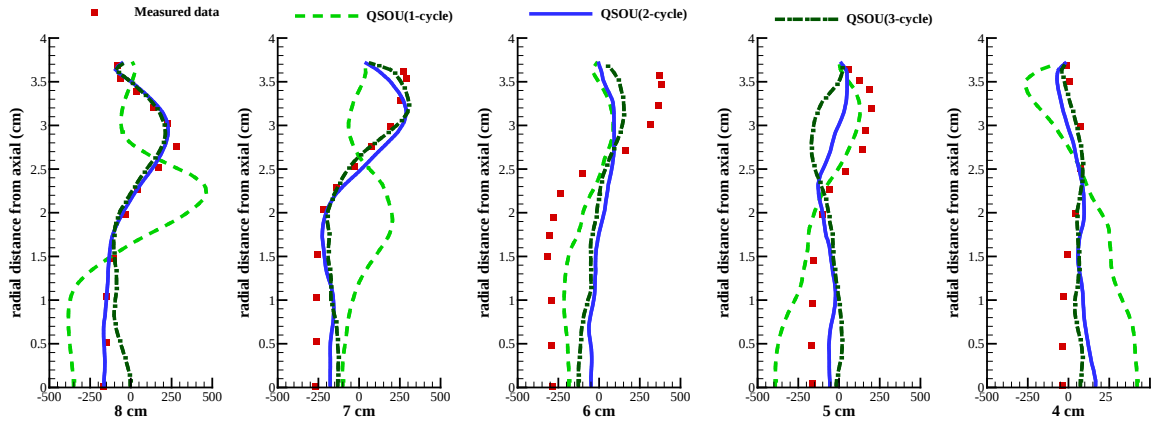

579

580 2 b) Predictions by QSOU Scheme ATDC 144°

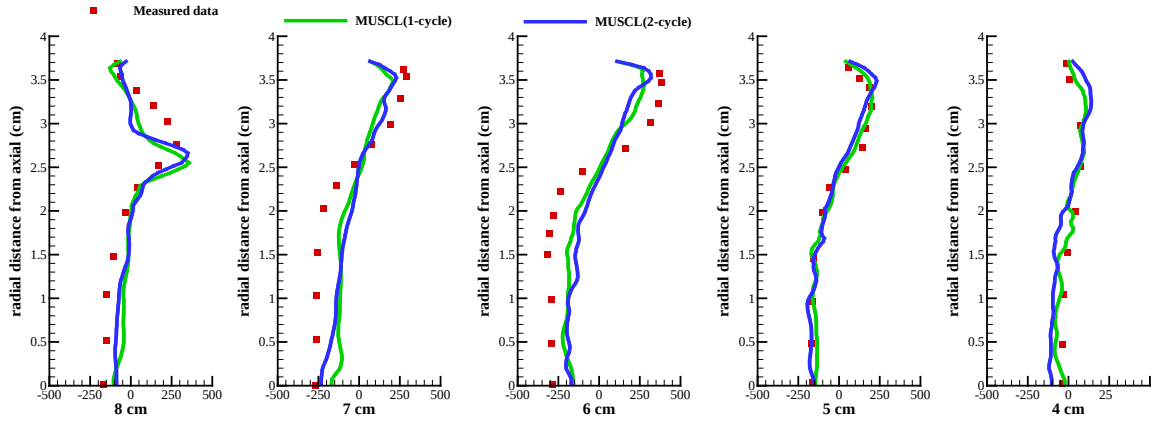

581

582 2 c) Predictions by MUSCL Scheme ATDC 144°

583 Axial mean velocity(cm/s)

584 Fig.2 Radial distribution of axial mean velocity at crank angle of ATDC 36° and ATDC 144°

585

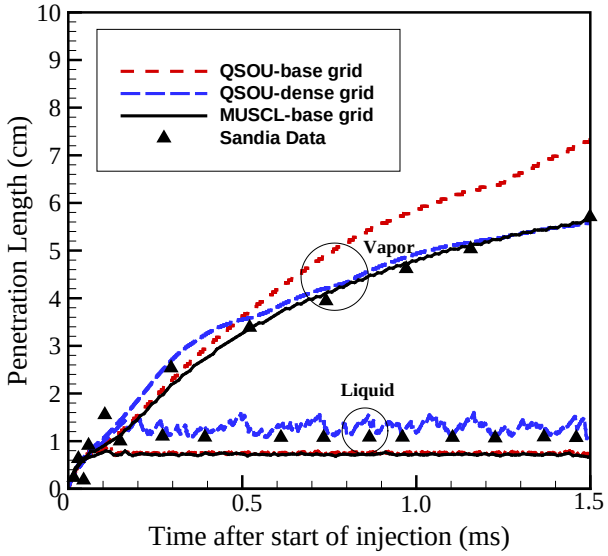

586

3 a) Penetration length variation with time after fuel injection

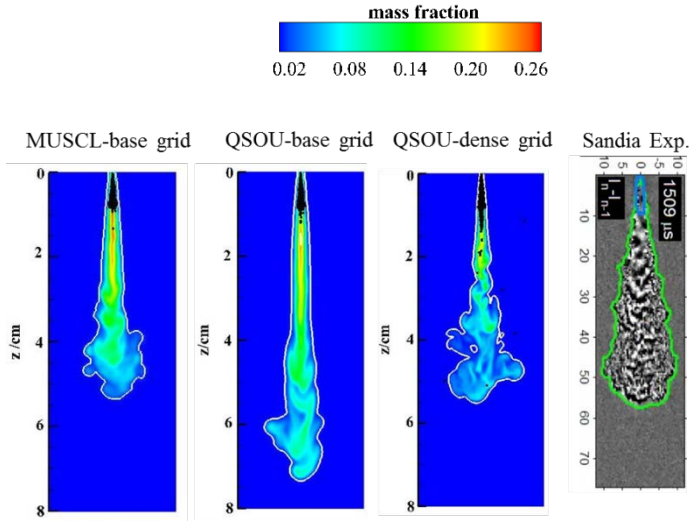

3b) Liquid and vapor mass fraction distribution

Fig. 3 Measured and predicted penetration length and fuel mass fraction at 1.5 ms for liquid and vapor phase using MUSCL and QSOU on base grid (about 800,000 cells) and dense grid (about 6 million cells) for Case 1

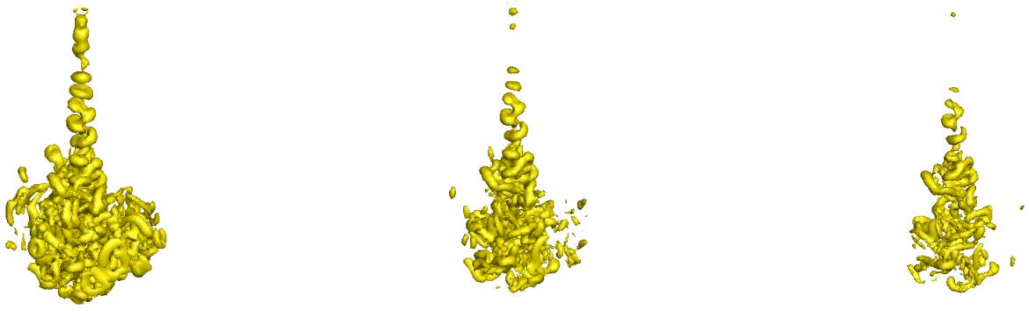

MUSCL with base grid

QSOU with base grid

$Q=1.5*10^7$ $Q=1.5*10^8$ $Q=4.5*10^8$

Fig.4 The vortex field at 1.5ms after start of injection for MUSCL and QSOU schemes on the base grid (Case 1)

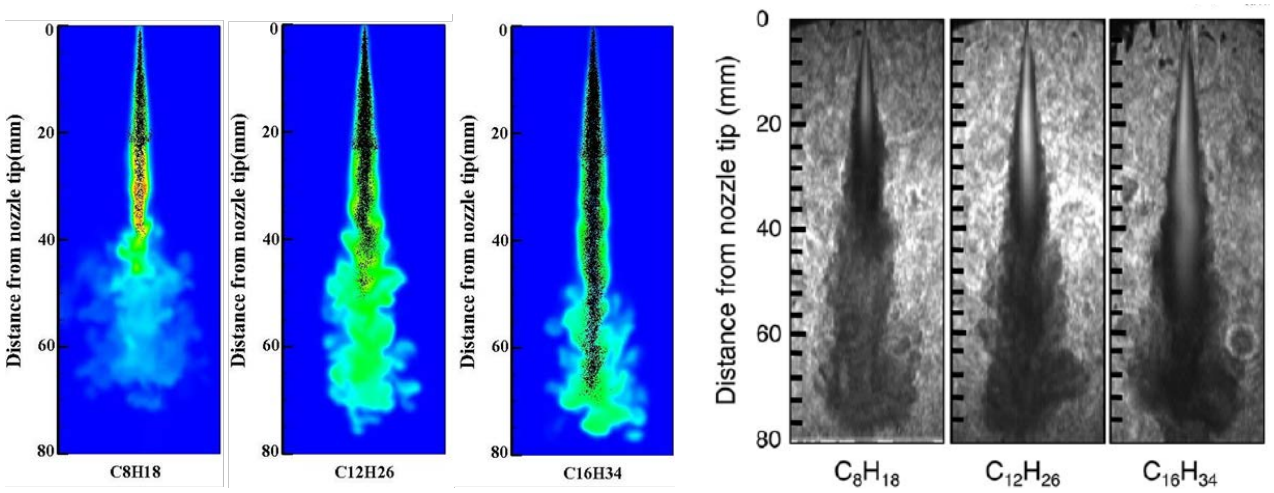

LES Exp.

Fig.5 Comparison of predicted results using LES and experiment images by Mie-scattered light and shadowgraph at the end of injection of 1.82ms for Case 2 (Ref.[20])

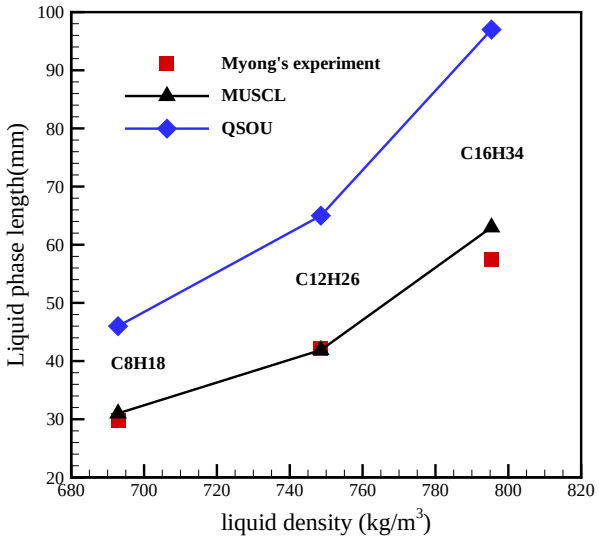

Fig. 6 Liquid phase length obtained through simulation using MUSCL and QSOU and experiment at different fuel densities for Case 2.

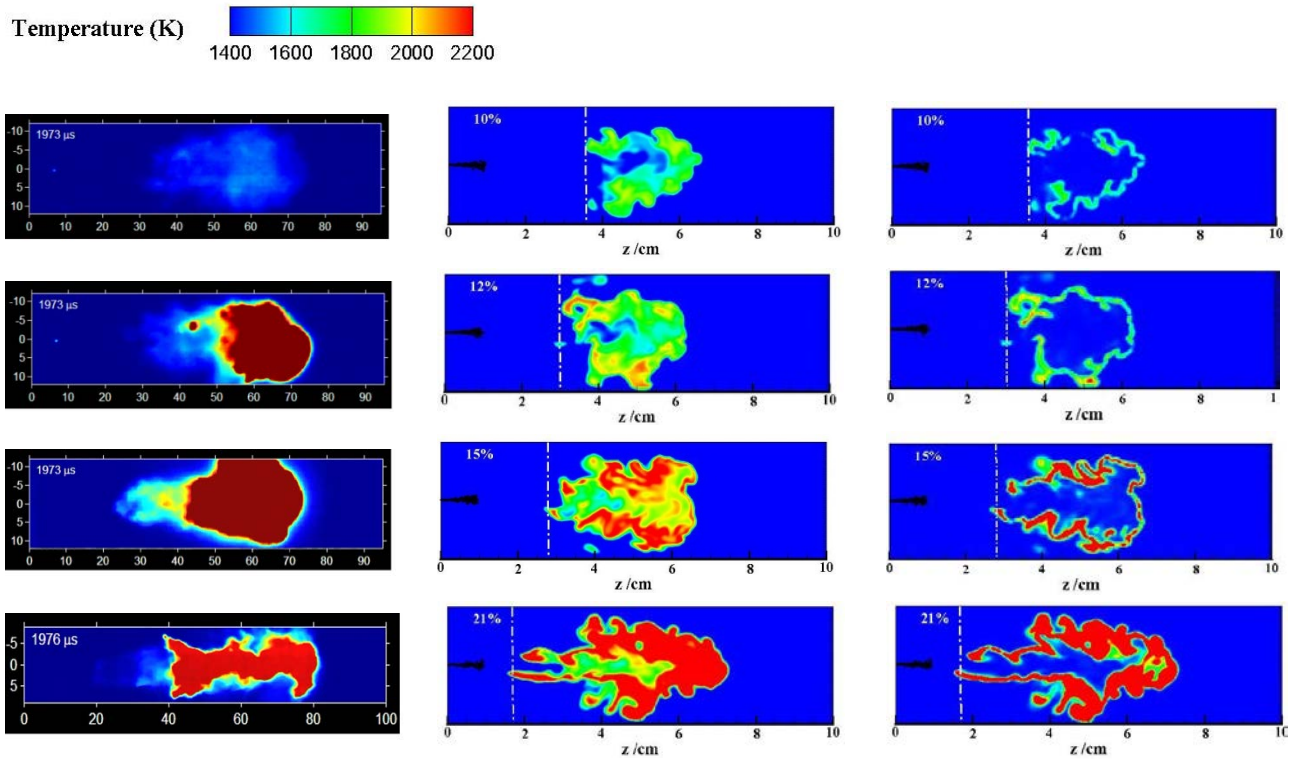

Sandia chemiluminescence image Temperature OH radical

Fig.7 Measured and predicted temperature and OH contours under different EGR at 2.0 ms ASOI for Case 3 (ambient density14.8 kg/m^3, ambient initial temperature1000 K). Dashed white line indicates the flame lift-off length.

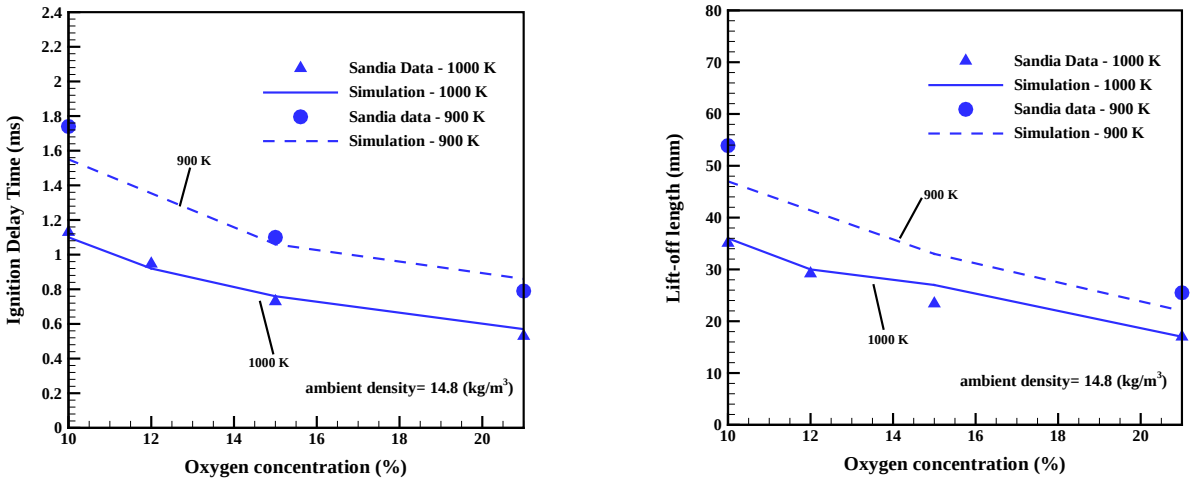

Fig.8 Measured and predicted ignition delay and flame lift-off length at different EGR for Case 3 (ambient density=14.8kg/m^3, ambient initial temperature=900 K and 1000K)

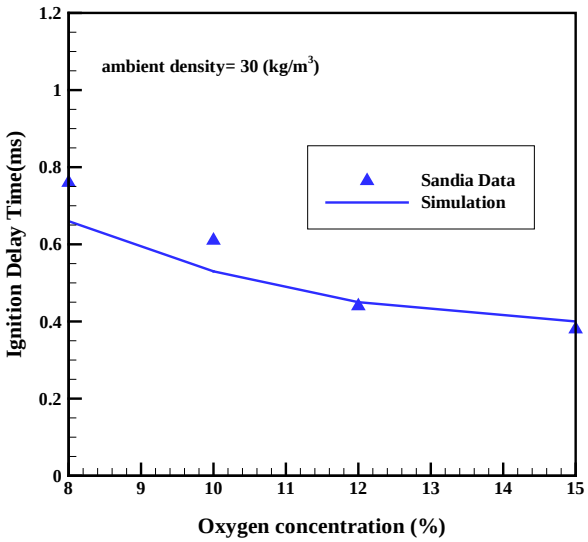

Fig. 9 Measured and predicted ignition delay time under different oxygen concentrations (ambient density 30.0 kg/m^3, ambient initial temperature 1000K).

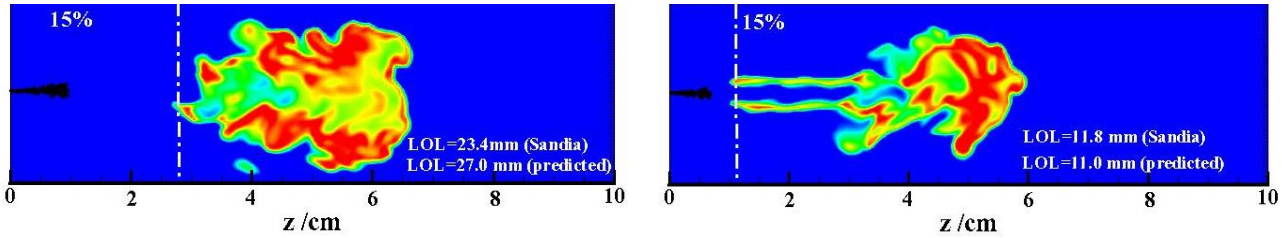

10 a) ambient density=14.8 kg/m^3 10 b) ambient density=30.0 kg/m^3

Fig.10 Influence of ambient density on temperature distribution under oxygen concentration of 15% and ambient temperature of 1000 K

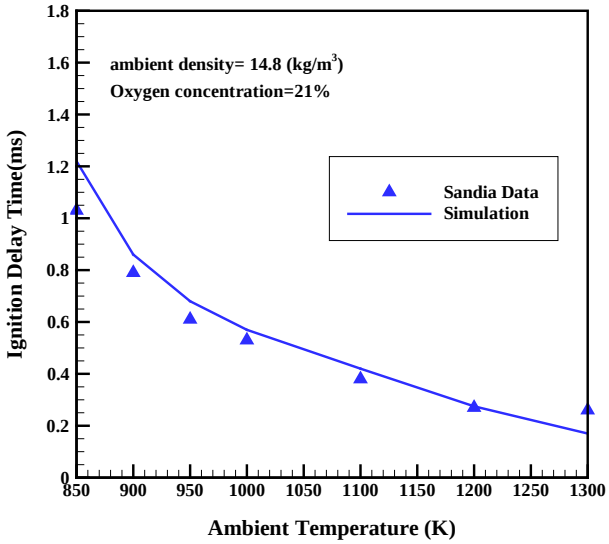

Fig.11 Measured and predicted ignition delay time at different ambient temperatures under oxygen concentration of 21% (ambient density=14.8 kg/m^3)